Research Article

Received: 28 June 2026
Accepted: 18 September 2026
Published: 13 November 2026

Green Synthesis, Characterization, and Antibacterial Efficacy of Zinc Oxide Nanoparticles Synthesized Using *Bougainvillea glabra* Leaf Extract

Mamoona Aleem
Department of Eastern Medicine, Faculty of Medical Sciences, Government College University, Faisalabad, Pakistan

Sabira Sultana (Corresponding Author)
Department of Eastern Medicine, Faculty of Medical Sciences, Government College University, Faisalabad, Pakistan;sabirasultana@gcuf.edu.pk

Beenish Ihsan
Faculty of Pharmacy, Chenab University of Sciences and Technology, Rahim Yar Khan, Pakistan

Ayesha Sarwar
Institute of Microbiology, Government College University, Faisalabad, Pakistan

Gull Naz
Institute of Microbiology, Government College University, Faisalabad, Pakistan

Rizwana Dilshad
Faculty of Pharmacy, Chenab University of Sciences and Technology, Rahim Yar Khan, Pakistan

Shehla Akbar
College of Pharmacy, University of Sargodha, Sargodha, Pakistan

Fajar Abbas
Institute of Microbiology, Government College University, Faisalabad, Pakistan

Cite this article:

M. Aleem (2026). Green Synthesis, Characterization, and Antibacterial Efficacy of Zinc Oxide Nanoparticles Synthesized Using *Bougainvillea glabra* Leaf Extract. Revista Cultura Científica, (24), pp. 2593–2606.
https://doi.org/10.70517/revcc2624208

2026 © The Author(s). Published by Revista Cultura Científica. This article is published as open access under the Creative Commons Attribution 4.0 International (CC BY 4.0) license (http://creativecommons.org/licenses/by/4.0/).

Abstract

This study evaluates the physicochemical characteristics, antioxidant activity, and antibacterial properties of zinc oxide preparations synthesized using *Bougainvillea glabra* leaf extract. The preparations were examined using a Zetasizer, scanning electron microscopy (SEM), X-ray diffraction (XRD), and Fourier transform infrared (FTIR) spectroscopy. An aluminum chloride assay was described for total flavonoid content (TFC), although a quantitative TFC result was not supplied. Antioxidant activity was assessed using the DPPH radical-scavenging assay, and antibacterial activity was examined by agar well diffusion against three bacterial species. Dynamic light scattering yielded an average hydrodynamic diameter of 218.6 nm, a polydispersity index of 0.242, and a zeta potential of -30.20 mV. SEM images showed irregular, agglomerated structures; the reported micrometer-scale features should not be interpreted as primary nanoparticle dimensions. The FTIR spectrum contained bands tentatively associated with organic functional groups. The reported XRD peaks occurred at 33.3° and approximately 60.0°, and a Scherrer calculation using the supplied peak width gave a crystallite-size estimate of approximately 83 nm. These observations alone do not establish crystal phase or phase purity. The maximum reported DPPH inhibition was 62.436%, and bacterial inhibition zones ranged from 15 to 20 mm. The antibiotic control is identified inconsistently as polymyxin B in the method and ciprofloxacin in the results, requiring confirmation. The reported microdilution tables contain arithmetic discrepancies: the original maximum means of 4.203 and 5.129 do not match their constituent measurements. Recalculated means are therefore presented alongside the original entries, without interpreting these measurements as validated minimum inhibitory concentrations. Overall, the observations support preliminary in vitro antioxidant and antibacterial activity under the reported conditions, while the concentration units, antimicrobial endpoints, and structural assignments require clarification before therapeutic conclusions can be drawn.

Keywords: Nanoparticles, Green synthesis, *Bougainvillea glabra* leaves, Zetasizer, Antibacterial activity, Antioxidant activities.

1. INTRODUCTION

Nanoparticles have become important in modern research across several scientific disciplines because of their distinctive physical, chemical, and biological properties. Primary nanoparticles conventionally have dimensions of approximately 1–100 nm, rather than micrometers, although suspensions can contain larger aggregates or agglomerates. Fakhari et al. [1] compared green routes for synthesizing zinc oxide nanoparticles and provide a relevant basis for considering how preparation conditions influence the resulting material. Applications of nanomaterials are investigated in medicine, materials science, electronics, and environmental science. Akinlotan and Ezenobi [2] reviewed different nanoparticle synthesis methods and their applications, providing general methodological context rather than direct evidence of improved bioavailability for the present formulation. Reduced dimensions can increase accessible surface area, but absorption, solubility, and stability depend on the material and its biological environment. Al-Ghamdi et al. [3] examined the antioxidant, antibacterial, and anticancer activity of zinc oxide nanoparticles prepared using *Camellia sinensis* tea leaf extract. Alamdari et al. [4] investigated the preparation and characterization of zinc oxide nanoparticles using *Sambucus ebulus* leaf extract, including their antibacterial and photocatalytic properties. These studies motivate plant-assisted synthesis without establishing controlled drug release or clinical safety for all preparations. Plant-derived constituents may participate in surface stabilization, but their presence does not by itself demonstrate biocompatibility. Abdelghany et al. [5] characterized willow-mediated zinc oxide nanoparticles and evaluated their antioxidant, anticancer, and antimicrobial activities. Their work illustrates the need to assess material properties and biological effects together rather than assume that a plant-assisted synthesis route guarantees compatibility with biological systems.

The antimicrobial and antioxidant properties of zinc oxide nanoparticles prepared in conjunction with medicinal plants have attracted considerable research interest. Agarwal et al. [6] reviewed plant-assisted approaches to zinc oxide nanoparticle synthesis and discussed their environmental and practical significance. Zinc oxide nanoparticles have been investigated for applications in agriculture, drug delivery, wound care, biosensing, pollutant degradation, and antimicrobial materials. Proposed uses in food packaging, coatings, and textiles depend on formulation-specific activity, exposure, and safety. Such applications should be distinguished from demonstrated performance of the material examined here. Adam et al. [7] prepared zinc oxide nanoparticles using *Moringa oleifera* water extract and evaluated photocatalytic activity; this supports the relevance of botanical synthesis routes but does not establish antioxidant synergy in the present samples. Rameshraddy et al. [8] examined zinc uptake, translocation, growth, yield, and moisture-stress tolerance in rice following zinc oxide nanoparticle treatment. Rizwan et al. [9] critically reviewed the effects of metal and metal oxide nanoparticles on food crops, emphasizing a broader range of physiological responses rather than universal benefits. Faizan et al. [10] reviewed zinc oxide nanoparticles in relation to plant growth and abiotic-stress alleviation. Venkatachalam et al. [11] investigated zinc oxide nanoparticles in *Leucaena leucocephala* seedlings exposed to heavy-metal stress. These agricultural studies provide background for possible future applications, but they are not evidence that the current preparation improves germination or stress tolerance. Antioxidant responses also depend on assay conditions and cannot be inferred solely from the electronic structure or surface characteristics of a nanoparticle. Agarwal and Shanmugam [12] reviewed anti-inflammatory mechanisms of green-synthesized zinc oxide nanoparticles; their review concerns anti-inflammatory activity and should not be treated as proof of efficacy against neurodegenerative disease. The tea-extract study by Al-Ghamdi et al. [3] offers more directly relevant in vitro biological evidence. Nevertheless, therapeutic applications require separate toxicity, exposure, and efficacy studies, and chemical radical-scavenging activity alone cannot establish protection from oxidative damage in living tissues.

Bougainvillea glabra, a member of the Nyctaginaceae family, is widely recognized for its ornamental value and has also been investigated for medicinal properties. Saleem et al. [13] reviewed its botany, traditional uses, phytochemistry, pharmacology, and toxicity. Common names vary regionally and include paper flower, bougainvillea, and lesser bougainvillea. Traditional uses and experimental reports motivate investigation of the plant but do not establish clinical efficacy. Sahu and Saxena [14] reviewed *B. glabra* as a potential source of natural antioxidants, providing background for examining radical-scavenging activity. Abarca-Vargas and Petricevich [15] reviewed the phytochemistry, pharmacology, and toxicology of the Bougainvillea genus and discussed phenolic compounds, flavonoids, terpenes, and betalains among its reported constituents. The occurrence and abundance of these constituents depend on species, cultivar, plant part, and extraction conditions; their presence in the current leaf extract was not established by compound-specific analysis. Plant constituents can participate in metal-ion complexation, particle formation, and surface capping, although the reaction mechanism should not be assumed from botanical identity alone. Samzadeh-Kermani et al. [16] previously synthesized zinc oxide nanoparticles using *B. glabra* leaf extract and investigated size distribution and antibacterial activity. Thus, the use of this plant for zinc oxide synthesis is not itself unprecedented. Oves et al. [17] investigated silver nanomaterial synthesized using *B. glabra* paper flowers and evaluated therapeutic applications; this is related botanical context, but silver particles and flower extracts cannot be treated as equivalent to the present zinc oxide and leaf-extract preparation. The present work therefore examines a particular preparation procedure and its physicochemical and in vitro biological observations. Its

objectives are to describe synthesis efficiency, characterize the resulting material, and assess antioxidant and antibacterial activity. Agricultural applications, including crop enhancement, stress management, and plant–nanoparticle interactions, remain prospective uses that require dedicated experiments. No plant-growth or stress-tolerance bioassay is documented in this study. Zinc oxide preparations were synthesized using *B. glabra* leaf extract, characterized using complementary methods, and examined in radical-scavenging and bacterial inhibition assays, with the interpretation restricted to the measurements actually reported.

2. MATERIALS AND METHODS

Bougainvillea glabra leaves were collected from mature plants in the local area of Faisalabad, Pakistan, for the preparation of zinc oxide nanoparticles. The plant material was identified and authenticated by the Department of Botany, Government College University Faisalabad.

Fresh leaves were washed with tap water followed by distilled water. Approximately 1 kg of fresh leaves was ground using a grinder. The resulting mixture was stirred for 1 h at 60 °C and subsequently soaked in 300 mL of ethanol for 48 h. The extract was filtered using a Büchner funnel and Whatman No. 1 filter paper.

Fresh ethanolic *Bougainvillea glabra* leaf extract (300 mL) was prepared and added to 100 mL of 0.02 M zinc acetate in ethanol at room temperature. This extract volume was used to promote distribution of the reaction components. The mixture was stirred for 20 min, after which 100 mL of sodium hydroxide solution was added dropwise. The resulting creamy green mixture was stirred for a further 2 h. Once the mixture had reached room temperature, it was transferred to centrifuge tubes, which were balanced in opposing rotor positions and centrifuged for 30 min. The resulting gel was transferred to a Petri dish and dried in a vacuum oven at 80 °C for 6 h. The reported powdered-product yield was 98% with fresh-leaf extract and 80% with dried-leaf extract. The yield calculation basis, sodium hydroxide concentration, centrifugation speed, and separate dried-leaf preparation conditions were not specified, so these percentages remain reported yields rather than independently verified mass balances.

Characterization of the preparations synthesized using *Bougainvillea glabra* leaf extract involved examining their particle-size distribution, electrokinetic properties, surface morphology, diffraction pattern, and infrared absorption bands. These complementary measurements describe different material properties and should not be interpreted as interchangeable estimates of particle size or biological efficacy.

The Zetasizer Nano series can measure particle size, zeta potential, and molecular weight in liquid media. All equipment was cleaned before analysis. The sample was dispersed in a solvent and mixed to improve uniformity, then passed through a 0.45 μm syringe filter. A volume of 0.5–1.0 mL of the *Bougainvillea glabra*-derived zinc oxide suspension prepared with sodium hydroxide was loaded into the cuvette. The solvent identity and detailed dispersion procedure were not specified.

After instrument calibration, the sample was introduced into a clean cuvette, with care taken to avoid bubbles. Measurement parameters, including refractive index and temperature, were entered into the software. Scattered-light measurements were analyzed to obtain the particle-size distribution, Z-average hydrodynamic diameter, and polydispersity index (PDI). For zeta-potential measurement, the sample was diluted and transferred to a cleaned measurement cell. The relevant viscosity and temperature parameters were set, and an electric field was applied to determine electrophoretic mobility and estimate zeta potential. Numerical values for the dispersant properties, dilution factor, pH, and measurement temperature were not supplied and should be retained in the experimental record for reproducibility.

The synthesized material was collected and prepared for scanning electron microscopy (SEM). The reported preparation involved fixation and dehydration to preserve the sample during imaging, followed by critical-point drying to reduce structural damage. The dried material was attached to a conductive substrate to improve electrical conduction and minimize charging. The prepared sample was introduced into the microscope chamber, which was evacuated before imaging. Instrument settings included the accelerating voltage, beam current, spot size, and working distance, with adjustments intended to provide suitable imaging resolution for the surface morphology of the *Bougainvillea glabra*-derived preparation. Secondary-electron imaging was selected to obtain topographical information. Focus and stigmation were adjusted to improve image clarity, and images were acquired at several magnifications to document the visible surface structures and agglomeration. The image annotations indicate an accelerating voltage of 10.0 kV. The method description also reports energy-dispersive X-ray spectroscopy (EDS) in conjunction with SEM for elemental analysis, together with image processing to quantify particle characteristics. However, an EDS spectrum, elemental composition table, particle-counting procedure, and size-distribution analysis were not included in the supplied results. Accordingly, elemental purity and primary-particle dimensions cannot be established from the available SEM images alone. The fixation reagents, coating conditions, critical-point drying settings, and quantitative image-analysis parameters require fuller documentation. The recovered images support qualitative examination of morphology, whereas the additional methodological steps remain descriptions requiring confirmation from the laboratory record.

X-ray diffraction (XRD) was used to examine the crystalline structure of the *Bougainvillea glabra*-derived zinc oxide preparation. The sample was spread uniformly in a holder, and the instrument was calibrated using a standard reference

material. Cu Kα radiation was used, and diffraction data were collected over a range of 2θ angles. The reported procedure involved comparison with JCPDS reference patterns, peak fitting, and peak-broadening analysis to estimate crystallite size. Crystallinity was described as being assessed from peak intensities relative to the total curve area; however, the reference-card identifiers, detailed acquisition settings, fitted peak parameters, and calculated crystallinity fraction were not supplied.

Fourier transform infrared (FTIR) spectroscopy was used to examine functional groups associated with the *Bougainvillea glabra*-derived preparation. The sample was mixed with potassium bromide (KBr) and pressed into a translucent pellet. After instrument calibration, a reference spectrum was recorded using a KBr pellet without sample. The sample spectrum was then acquired, the reference contribution was subtracted, and absorption bands were examined for tentative functional-group assignments.

Antioxidant activity was evaluated using the DPPH radical-scavenging assay. Three milliliters of sample were mixed with 1 mL of 0.004% DPPH solution, incubated in the dark for 30 min, and measured at 520 nm. Percentage inhibition was calculated relative to the blank absorbance. The original procedure proposed determining the concentration producing 65% inhibition (IC_{65}) from the inhibition–concentration relationship. However, the reported maximum inhibition was below 65%, and the sample-level units do not define a concentration series; consequently, an IC_{65} cannot be established from the available measurements.

Total flavonoid content (TFC) was assessed using an aluminum chloride assay. A 0.5 mL aliquot of sample was mixed with 2 mL of distilled water, followed by sequential additions of 5% sodium nitrite ($NaNO_2$), 10% aluminum chloride ($AlCl_3$), and sodium hydroxide. The final volume was adjusted to 5 mL with methanol, and the mixture was incubated for 15 min. Absorbance was measured at 510 nm. A catechin calibration curve was specified for expressing TFC as micrograms of catechin equivalents per milligram of extract, although the calibration data and final TFC value were not reported.

Antibacterial activity against *Escherichia coli*, *Pseudomonas aeruginosa*, and *Staphylococcus aureus* was evaluated by agar well diffusion. A 100 μL bacterial suspension containing 10^7 CFU/mL was spread on Mueller–Hinton agar. Polymyxin B was specified as the positive control in the method description. After refrigeration for 2 h and incubation at 37 °C for 18 h, inhibition-zone diameters were measured. The results identify ciprofloxacin as the control instead; the antibiotic identity therefore requires confirmation before the comparison can be interpreted conclusively.

The microdilution assay was intended to determine the lowest nanoparticle concentration inhibiting bacterial growth. Bacterial cultures were incubated overnight and centrifuged for clarification, as described in the original procedure. Serial dilutions of test substances were added to 96-well plates containing Mueller–Hinton broth and bacterial suspensions. Ciprofloxacin was used as the positive control. Plates were incubated at 37 °C for 24 h. The proposed minimum inhibitory concentration (MIC) endpoint was the lowest concentration without detectable bacterial growth, assessed from changes in the medium. The dilution concentrations, final inoculum, growth and sterility controls, and any color indicator were not specified, limiting validation of the reported endpoint.

3. RESULTS AND DISCUSSION

Zinc oxide preparations were produced using *Bougainvillea glabra* leaf extract and examined by physicochemical and biological methods. The reported measurements indicate in vitro bacterial growth inhibition and DPPH radical scavenging under the stated conditions. Zeta potential and light scattering describe the dispersed material, while XRD, SEM, and FTIR provide complementary information about diffraction features, visible morphology, and infrared-active groups. These methods do not independently establish therapeutic efficacy or confirm every structural assignment. No inferential statistical analysis or uncertainty estimates were supplied for the biological comparisons. The findings are therefore described as observed activities, with attention to discrepancies in particle-size interpretation, assay units, and microdilution arithmetic.

Zeta potential and particle-size distribution were measured using a Zetasizer. Table 1 summarizes the reported electrokinetic and size parameters, and Figure 1 presents the intensity-weighted size distribution. Zeta potential describes the electrokinetic behavior of the dispersed material, whereas the hydrodynamic diameter includes contributions from solvation, surface-associated material, and any agglomeration present during measurement.

Table 1. *Zeta Potential and Hydrodynamic Size Parameters.*

Parameter	Value
Zeta potential (mV)	-30.20
Average Particle size (nm)	218.6
Polydispersity Index (PDI)	0.242

The measured zeta potential was -30.20 mV, as reported in Table 1. Its negative sign indicates negative electrokinetic potential under the measurement conditions. A magnitude of approximately 30 mV is often interpreted as consistent with

appreciable electrostatic repulsion, but it is not an unconditional guarantee of colloidal stability. Aggregation also depends on pH, ionic strength, dispersant composition, concentration, and the duration of observation. Because these conditions and time-dependent stability measurements were not reported, the preparation should be described as having the measured negative zeta potential rather than as proven resistant to aggregation in every aqueous environment.

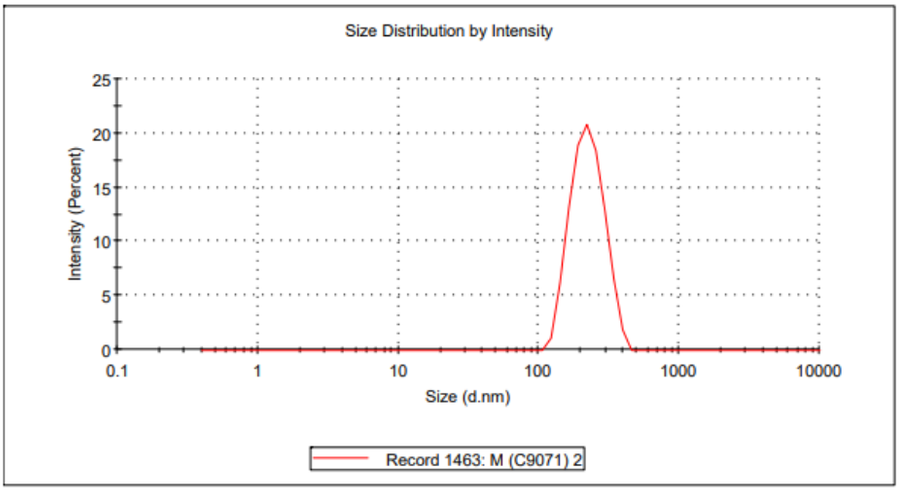


Figure 1. *Intensity-Weighted Hydrodynamic Size Distribution.*

The reported average hydrodynamic diameter was 218.6 nm, with a PDI of 0.242 (Table 1). The PDI describes the breadth of the light-scattering distribution and is consistent with a moderately limited distribution under the stated measurement approach. However, the intensity distribution in Figure 1 can be strongly influenced by larger scattering entities. These measurements do not by themselves establish that all primary particles have the same size.

The hydrodynamic diameter of 218.6 nm should be distinguished from the approximately 83 nm crystallite-size estimate obtained from the reported XRD calculation. A hydrodynamic diameter describes dispersed entities, whereas a Scherrer estimate concerns coherent diffracting domains. Different values are therefore possible without implying an analytical contradiction. The original attribution of approximately 219 nm to XRD was inconsistent with the later calculation and has been corrected. Further dispersion characterization and independent particle imaging would be needed before size uniformity could support a specific biomedical application.

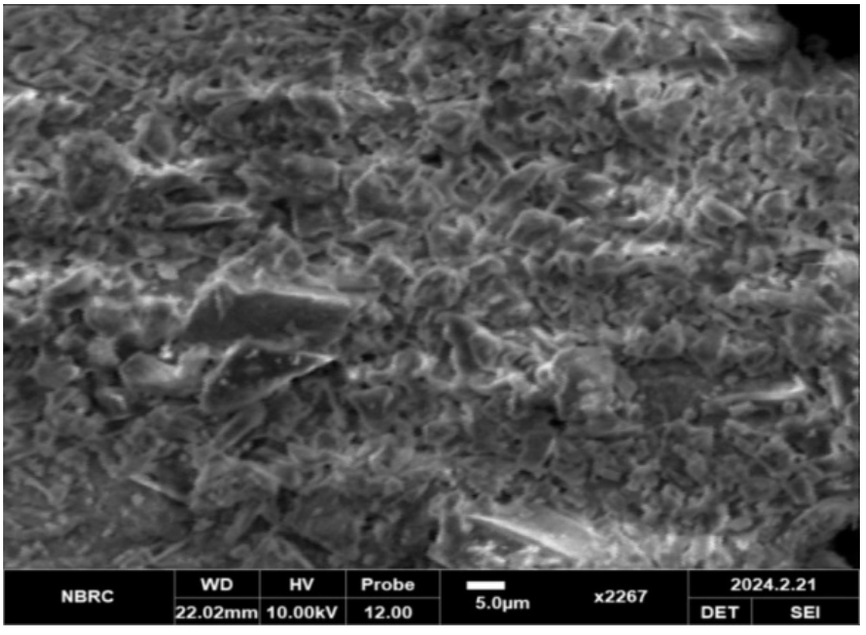
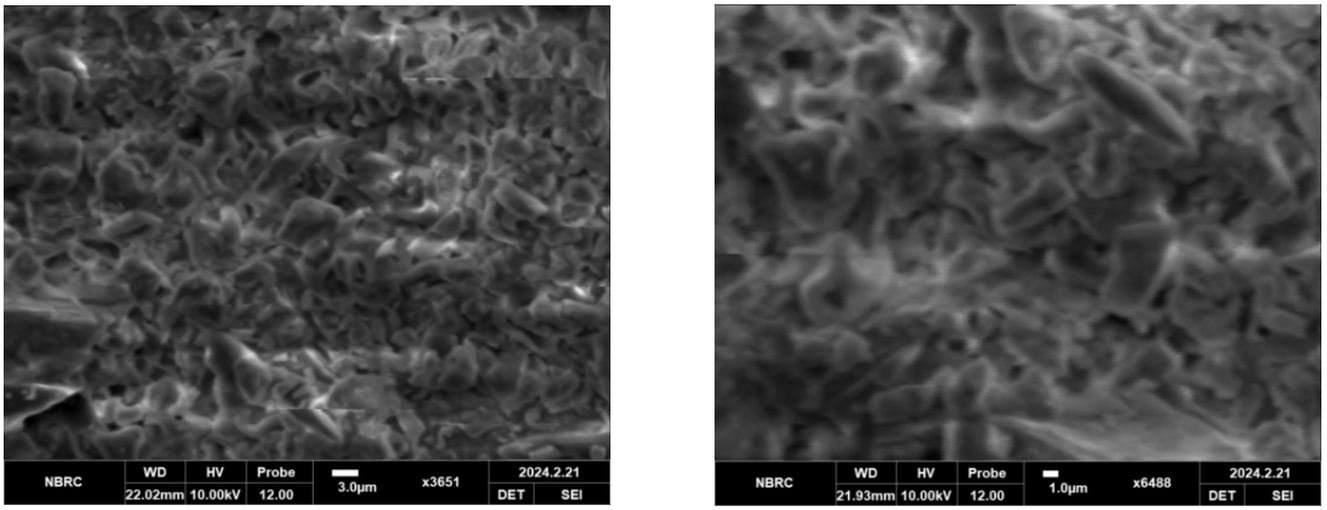


Figure 2. *SEM Image Acquired at ×2267.*

Scanning electron microscopy uses a focused electron beam to generate signals from the sample surface and provide information about morphology and topography. The supplied micrographs show irregular structures, porous regions, and agglomeration. The original description gives feature dimensions of 20–28 μm, which refer to micrometer-scale structures rather than primary nanoparticles. These estimates are not supported by a documented particle-counting analysis and

should be treated as qualitative observations requiring confirmation.

The micrograph in Figure 2 was acquired at ×2267, while Figure 3 presents images at ×3651 and ×6488; all are annotated at 10.0 kV. Irregular and agglomerated structures are visible. The scale bars of 3.0 μm and 1.0 μm in Figure 3 are image reference lengths, not measured mean particle diameters. The original estimate of 22–28 nm conflicts with the accompanying micrometer-scale description and cannot be confirmed from these images alone. Aggregation during preparation or drying is a possible explanation for the visible structures, but its dependence on ethanol was not experimentally isolated. The magnification label ×3651 is retained as shown in the supplied image.



(a) (b)

Figure 3. *SEM Images at (a) ×3651 and (b) ×6488.*

The SEM images show morphology and agglomeration but do not establish a concentration-dependent change in crystallinity. The reported 20–24 μm porous features cannot be converted into an individual-particle size of 20–24 nm without an independent measurement. Similarly, the original Figure 3 annotation referred to annealing at 400 °C, whereas the synthesis method reports drying at 80 °C. The thermal history of these images therefore remains unresolved. XRD provides separate diffraction information, but neither these micrographs nor the reported peak list establishes the claimed concentration effect.

X-ray diffraction provides information about crystalline structure through the positions and profiles of diffraction peaks. The supplied pattern is shown in Figure 4, with reported peaks at 2θ = 33.3° and approximately 60.0°. These features indicate diffraction from the preparation, but the two reported positions alone are insufficient for reliable phase identification. The original assignment to the "110 and 90" planes of cubic ZnO is not a validated crystallographic indexing and should not be used to establish crystal symmetry.

The crystal phase and phase purity cannot be confirmed from the available two-peak description and unindexed trace. Alamdari et al. [4] identified a wurtzite structure in a different plant-mediated ZnO preparation using XRD characterization; this provides relevant comparative context rather than proof of the phase present here. A complete indexed pattern, reference-card identifiers, and assessment of possible secondary phases are required before the current sample can be described as cubic, phase-pure, or impurity-free.

The crystallite-size estimate was obtained using the Scherrer equation, with the peak width expressed in radians:

$$D = \frac{K\lambda}{\beta \cos\theta}. \tag{1}$$

The symbols in Eq. 1 are defined as follows: D is the coherent crystallite-size estimate; K is the assumed shape factor, taken as 0.9; λ is the X-ray wavelength, 1.5406 Å (0.15406 nm) for Cu Kα radiation; β is the full width at half maximum in radians; and θ is the Bragg angle, equal to half the reported 2θ value.

For the reported peak at 2θ = 33.3°, θ = 16.65° and the supplied FWHM of 0.1° corresponds to approximately 0.001745 rad. Substitution into Eq. 1 gives approximately 82.92 nm, consistent with the originally reported estimate of 82.96 nm at the precision justified by the peak width. Instrumental broadening and lattice-strain contributions were not provided, so the result is an approximate coherent-domain estimate rather than an independently validated particle diameter.

The calculation therefore suggests a characteristic diffracting-domain size of approximately 83 nm under the stated assumptions. It does not independently verify ZnO phase identity or establish suitability for antibacterial treatment, ultraviolet protection, drug delivery, wound healing, or cancer therapy. Such applications require additional material characterization, biological controls, and exposure-specific safety evaluation. The present diffraction estimate should be

interpreted together with, rather than substituted for, the separate light-scattering and microscopy observations.

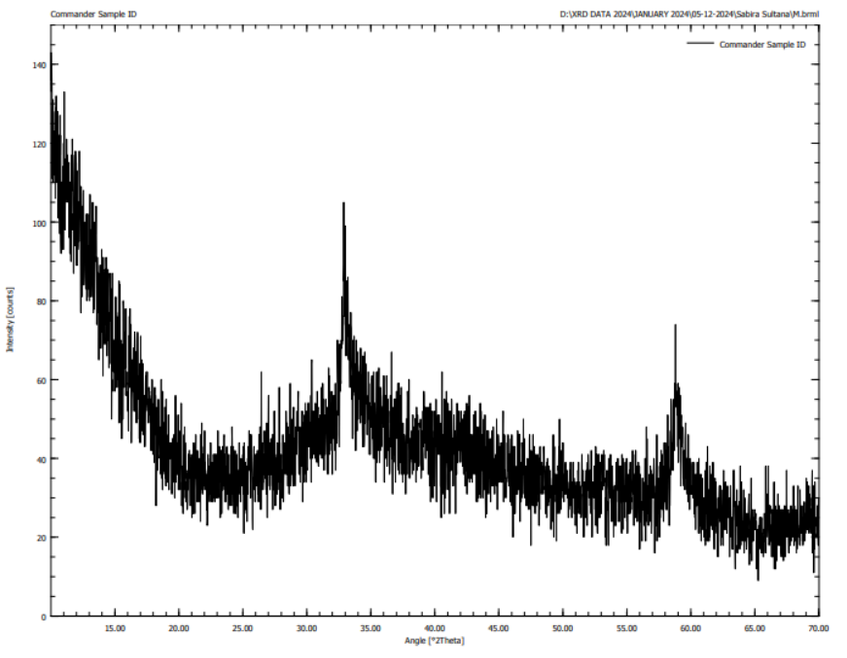


Figure 4. *Supplied X-Ray Diffraction Pattern.*

Small coherent-domain dimensions can influence optical, electronic, and mechanical properties, while accessible surface area also depends on particle morphology and agglomeration. Accordingly, the approximate crystallite-size estimate motivates further characterization but does not by itself demonstrate improved medicinal performance or a particular application-specific advantage.

Peak breadth can be influenced by crystallite size, instrumental resolution, and lattice strain. The available trace and single reported width do not separate these contributions. Consequently, minimal strain, low defect density, and a quantitatively high degree of crystallinity cannot be established solely from the apparent sharpness of the displayed peaks.

FTIR spectroscopy was used to examine infrared-active groups associated with the preparation and possible surface-bound organic material. The reported measurement range was 650–4000 cm^{-1}. The spectrum in Figure 5 provides information about absorption bands, but band positions alone do not identify individual biological compounds or prove a specific capping mechanism. Assignments are therefore treated as tentative functional-group interpretations.

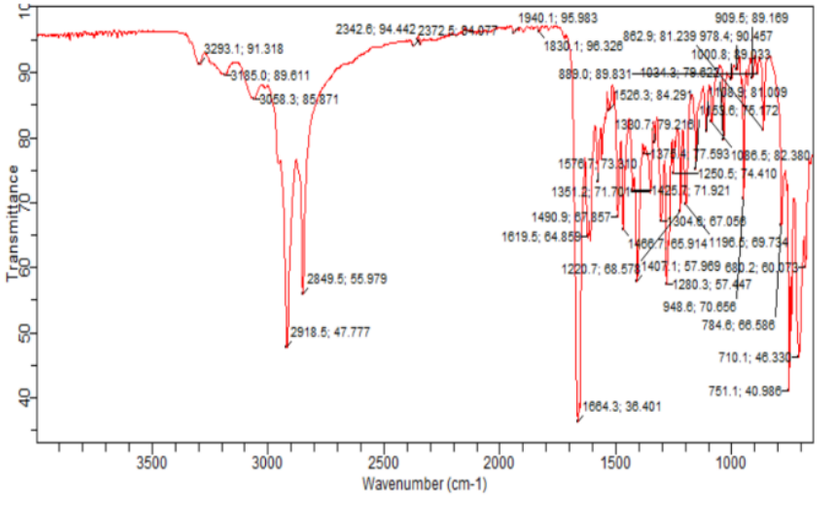


Figure 5. *FTIR Spectrum of the Leaf-Extract-Mediated Preparation.*

The FTIR spectrum exhibits absorption features that may be associated with several functional groups. Table 2 retains the reported frequency ranges as a tentative assignment guide, with obvious bond-assignment inconsistencies corrected. These ranges overlap and should not be read as independent confirmation of every listed compound class.

A broad feature in the 3200–3500 cm^{-1} region is consistent with O–H stretching, commonly associated with alcohols, phenols, or adsorbed water. The feature therefore suggests hydroxyl-containing material associated with the preparation, although it does not distinguish plant-derived hydroxyl groups from residual moisture.

Absorption in the 3000–3100 cm^{-1} region can be associated with unsaturated C–H stretching. This assignment is compatible with certain alkene or aromatic environments, but the band range alone does not establish a particular organic compound.

Absorption in the 2800–3000 cm^{-1} region is commonly associated with aliphatic C–H stretching, rather than the N–H stretching originally assigned in the text. Such features could arise from organic material associated with the particles or residual solvent; a solvent reference and appropriate controls would help distinguish these possibilities.

Features in the 1700–1750 cm^{-1} region are compatible with carbonyl (C=O) stretching. Possible contributing classes include esters, aldehydes, and carboxylic acids, although distinguishing among these possibilities requires additional spectral information and appropriate chemical characterization.

The 1550–1650 cm^{-1} region can include amide-related C=O and N–H vibrations as well as other overlapping absorptions. Assigning a specific lactam, protein, peptide, or nitro compound from this broad interval alone would be premature. These possibilities are therefore not treated as identified constituents of the capping layer.

The broad 1465–1690 cm^{-1} interval includes potential C–H bending, C=C stretching, N–H bending, and C=O stretching contributions. The original list also included N–O and C=N assignments. These overlapping possibilities illustrate why a general frequency guide cannot uniquely distinguish alkanes, unsaturated carbonyl compounds, amines, and other organic groups in a complex extract-derived sample.

The 1300–1450 cm^{-1} region can contain C–H and O–H bending contributions. Sulfur-containing functional groups were also proposed in the original interpretation, but no independent sulfur analysis was supplied. Consequently, assignments to sulfate, sulfonyl chloride, or related classes remain unconfirmed and should not be presented as detected constituents.

The 1000–1400 cm^{-1} region includes potential C–O stretching and overlapping vibrations associated with alcohols, ethers, and other oxygen-containing organic material. Although the original frequency guide also lists C–F stretching, that entry does not demonstrate the presence of fluorinated compounds. Element-specific evidence would be needed to substantiate such an assignment.

Overall, the FTIR observations are consistent with organic functional groups associated with the sample, but they do not identify individual active phytochemicals or their concentrations. The synthesis used an ethanolic leaf extract; the original reference to a methanolic extraction is therefore inconsistent with the preparation method, although methanol was separately specified in the TFC assay. Table 2 provides possible frequency assignments for interpretation, not a verified inventory of compounds in the preparation. Compound-specific identification would require additional separation or spectrometric measurements.

Table 2. *Tentative FTIR Frequency Assignments.*

Frequency (cm^{-1})	Tentative Vibration	Possible Class
3200-3500	o-h stretching	Alcohol
3000-3100	c-h stretching	Alkene
2800-3000	C–H stretching	Aliphatic hydrocarbon
1700-1750	c=o stretching	Esters, aldehydes, or carboxylic acids
1650-1550	Overlapping C=O/N–H vibrations	Amide-related groups (tentative)
1465	c-h bending	Alkane
1500-1550	n-o stretching	Nitro compound
1610-1620	c=c stretching	α-β- unsaturated ketone
1638-1648	c=c stretching	Alkene
1580-1650	n-h bending	Amine or amide (tentative)
1690	c=o stretching	Primary amide
1330-1420	o-h bending	Alcohol
1380-1385	c-h bending	Alkane
1380-1390	c-h bending	Aldehyde
1450	c-h bending	Alkane
1500-1550	n-o stretching	Nitro compound
1000-1400	c-f stretching	Fluoro compounds
1030-1070	s=o stretching	Sulfoxide
1050-1085	c-o stretching	Primary alcohol
1085-1150	c-o stretching	Aliphatic ether

Phytochemical literature reports several classes of compounds in Bougainvillea species, including phenolics and

flavonoids [15]. However, the current measurements do not independently establish the presence of triterpenoids, anthocyanins, ellagic acid, or isoquercetin in the tested preparation. DPPH inhibition was used to assess radical-scavenging behavior of the preparation as a whole, without attributing the measured response to any individually identified constituent.

The reported DPPH inhibition values ranged from 21.421% to 62.436% (Table 3). Figure 6 displays these percentages alongside the blank and sample absorbances. Maximum inhibition occurred at the reported sample level of 200 mL, followed by a lower value at 300 mL. The labels are retained exactly as supplied, but mL is a volume unit and does not define nanoparticle concentration. Because the assay method specifies only 3 mL of sample per reaction, the meaning of these level labels requires clarification before a concentration–response interpretation or IC_{65} calculation is attempted.

Table 3. *Reported DPPH Absorbance and Inhibition Values.*

Sample Level (mL)	Blank Absorbance	Sample Absorbance	Inhibition (%)
50	0.985	0.774	21.421
100	0.985	0.499	49.340
200	0.985	0.37	62.436
300	0.985	0.448	54.517

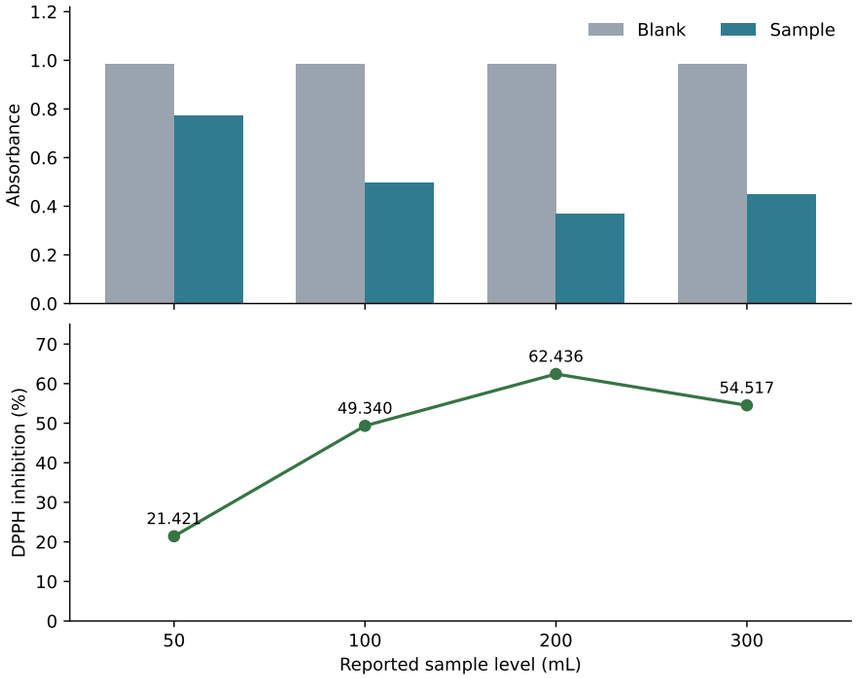


Figure 6. *DPPH Absorbance and Inhibition Across Reported Sample Levels.*

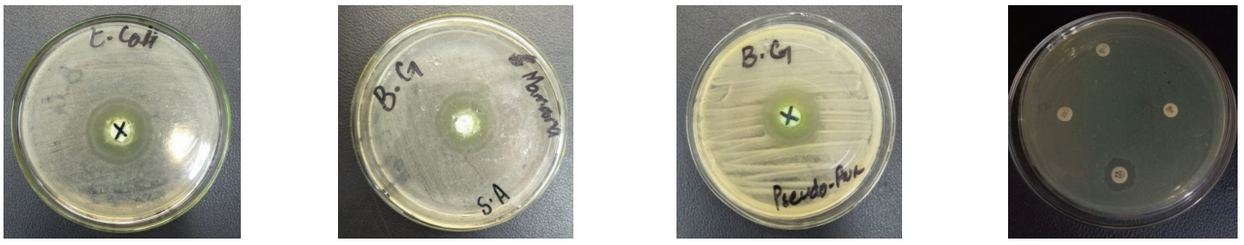
The aluminum chloride procedure was described for determining TFC, but no numerical flavonoid-content result or catechin calibration data were provided. An additional passage specified 0.5 mL of plant extract, 2 mL of ethanol, and a 5% $NaNO_2$ solution with an ambiguous volume written as "0.15 5 mL," followed by 6 min of incubation and addition of 0.15 mL of 10% $AlCl_3$ solution with a further 6 min incubation. That passage then described 222 mg of methionine, 0.0375 mL of a "Titan" reaction mixture, illumination at a reported 350 mol m^{-2} s^{-1} for 15 min, and inhibition of nitro blue tetrazolium reduction at 560 nm. The latter conditions concern a superoxide dismutase (SOD) assay, with one unit defined by 50% inhibition, and do not constitute a TFC measurement. These mixed protocol details require reconciliation with the experimental record; neither a TFC value nor SOD activity can be inferred from the available description.

Table 4. *Reported Bacterial Inhibition-Zone Diameters.*

Bacterial Species	Preparation (mm)	Antibiotic Control (mm)
Pseudomonas aeruginosa	20	24
Staphylococcus aureus	15	18
Escherichia coli	15	19

Antibacterial activity was examined against *Pseudomonas aeruginosa* and *Escherichia coli*, both Gram-negative bacteria, and *Staphylococcus aureus*, a Gram-positive bacterium. Table 4 gives the reported inhibition-zone diameters, and Figure 7 presents the supplied agar-plate images. The preparation produced a 20 mm zone against *P. aeruginosa* compared with a 24 mm antibiotic-control zone. The corresponding values were 15 and 18 mm for *S. aureus* and 15

and 19 mm for *E. coli*. Thus, all three reported preparation zones were smaller than their respective control zones. The results label the antibiotic as ciprofloxacin, whereas the method names polymyxin B; this discrepancy remains unresolved. Replication, uncertainty, well diameter, and applied nanoparticle dose were not supplied, so these observations do not establish statistical equivalence or relative potency against the antibiotic.



(a) (b) (c) (d)

Figure 7. *Agar Plates for (a) E. coli, (b) S. aureus, (c) P. aeruginosa, and (d) the Control.*

The microdilution experiment was intended to evaluate bacterial growth inhibition by the synthesized preparation against *S. aureus* and *E. coli* in 96-well plates. Tables 5 and 6 reproduce the three listed measurements for each isolate and retain the original reported mean beside an independently recalculated arithmetic mean. The first table is assigned to *S. aureus*; the second is assigned to *E. coli* following the abstract and accompanying narrative, although its original column heading incorrectly repeated *S. aureus*. This organism assignment requires confirmation against the plate record. Values originally labeled μg/mL cannot be accepted as validated MIC concentrations without the dilution series and endpoint documentation.

Table 5. *Reported S. aureus Microdilution Entries and Recalculated Means.*

Isolate	Value 1	Value 2	Value 3	Reported Mean	Recalculated Mean
MRS-1	1.302	1.413	1.102	1.272	1.272
MRS-2	1.800	1.900	1.510	4.203	1.737
MRS-3	1.652	1.762	1.614	1.676	1.676
MRS-4	1.771	1.871	1.543	1.728	1.728
MRS-5	1.678	1.788	1.699	1.721	1.722
MRS-6	1.760	1.814	1.682	1.752	1.752
MRS-7	1.702	1.809	1.624	4.052	1.712
MRS-8	1.620	2.059	1.540	1.739	1.740
MRS-9	1.344	1.544	1.244	1.377	1.377
MRS-10	0.587	0.694	0.590	0.623	0.624
MRS-11	1.028	1.062	1.309	1.133	1.133
MRS-12	0.005	0.986	1.667	0.886	0.886

Table 6. *Reported E. coli Microdilution Entries and Recalculated Means.*

Isolate	Value 1	Value 2	Value 3	Reported Mean	Recalculated Mean
MRS-1	1.204	1.305	1.102	1.200	1.204
MRS-2	1.613	1.724	1.513	1.616	1.617
MRS-3	1.602	1.713	1.814	5.129	1.710
MRS-4	1.671	1.782	1.543	4.990	1.665
MRS-5	1.478	1.689	1.699	1.622	1.622
MRS-6	1.460	1.571	1.682	1.571	1.571
MRS-7	1.822	1.934	1.624	1.793	1.793
MRS-8	1.620	1.720	1.540	1.626	1.627
MRS-9	0.344	0.488	0.244	0.285	0.359
MRS-10	1.826	1.937	1.590	1.784	1.784
MRS-11	1.228	2.449	1.309	1.662	1.662
MRS-12	1.005	2.115	1.667	1.595	1.596

The supplied microtitration plate is shown in Figure 8. According to the method description, absorbance was measured at 620 nm at the beginning of the experiment and after 24 h of incubation. Lower absorbance in the initial wells and increasing absorbance in later wells were interpreted as differences in bacterial growth. However, the plate map, blank correction, and correspondence between optical-density readings and concentration endpoints were not supplied. In Table 5, the original means of 4.203 for MRS-2 and 4.052 for MRS-7 are inconsistent with the listed measurements; their

recalculated means are 1.737 and 1.712. In Table 6, MRS-3, MRS-4, and MRS-9 have recalculated means of 1.710, 1.665, and 0.359, rather than 5.129, 4.990, and 0.285. Smaller rounding differences are also visible. These arithmetic corrections preserve the individual entries and improve internal consistency, but do not resolve whether the underlying values represent absorbance, concentration, or another reported quantity. Consequently, the originally claimed MIC rankings are not used as evidence of antibacterial potency.

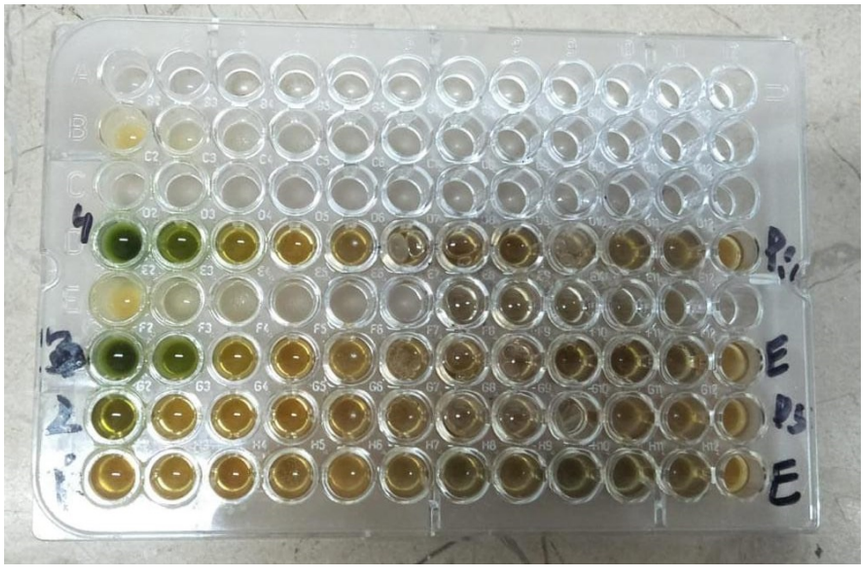


Figure 8. *Supplied Microdilution Plate Image.*

The present study documents physicochemical observations and in vitro assays; it does not document seed-germination, seedling-vigor, photosynthesis, or stress-tolerance experiments. The agricultural implications therefore remain prospective rather than demonstrated findings. Rizwan et al. [9] reviewed crop responses to metal and metal oxide nanoparticles, providing context for both beneficial and adverse effects. Faizan et al. [10] discussed zinc oxide nanoparticles in relation to growth and abiotic-stress tolerance. Venkatachalam et al. [11] examined a specific heavy-metal-stress experiment in Leucaena seedlings. Those investigations cannot validate a growth-promoting effect of the present Bougainvillea-derived preparation without comparable plant experiments. Possible mechanisms involving zinc availability, photosynthetic processes, and antioxidant defenses would need to be tested with dose controls and suitable measurements. Similarly, the Moringa-based photocatalytic work of Adam et al. [7] demonstrates a botanical preparation route rather than a plant bioassay for this material. Future agricultural evaluation would require dose optimization, assessment of nanoparticle fate in soil, long-term exposure studies, and examination of plant signaling responses before environmental safety or crop benefits could be claimed.

4. CONCLUSION

This study describes the preparation of a *Bougainvillea glabra* leaf-extract-mediated zinc oxide material and its preliminary in vitro antioxidant and antibacterial observations. Reported inhibition zones were 15–20 mm against *E. coli*, *S. aureus*, and *P. aeruginosa*, while maximum DPPH inhibition was 62.436% under the supplied assay labels. Light scattering yielded a hydrodynamic diameter of 218.6 nm and a zeta potential of -30.20 mV; the separate Scherrer calculation suggested a coherent-domain size of approximately 83 nm. SEM and FTIR provided qualitative morphological and functional-group information. The results do not establish clinical efficacy, improved plant growth, phase purity, or superiority to alternative extracts. Clarification of the antibiotic control, concentration units, microdilution endpoints, thermal history, and diffraction indexing is necessary before stronger conclusions are justified. The preparation warrants further controlled investigation, with arithmetic corrections retained transparently and therapeutic applications treated as possibilities requiring direct evaluation.

Author Contributions

All authors contributed equally to this study and to the preparation of the manuscript. All authors read and approved the final version for publication.

Conflicts of Interest

The authors declare no conflicts of interest.

Data Availability Statement

The aggregated data supporting the findings of this study are available from the corresponding author upon reasonable request.

Funding Information

No external funding was received for this research or for the preparation of the manuscript.

REFERENCES

[1] Fakhari, S.; Jamzad, M.; Kabiri Fard, H. (2019). Green synthesis of zinc oxide nanoparticles: a comparison. *Green Chemistry Letters and Reviews*, *12* (1), 19–24. https://doi.org/10.1080/17518253.2018.1547925.

[2] Akinlotan, O. O.; Ezenobi, U. V. (2020). A review of various methods of synthesizing nanoparticles and their applications. *Journal of Chemical Society of Nigeria*, *45* (4), 656–662. https://doi.org/10.46602/jcsn.v45i4.489.

[3] Al-Ghamdi, S. A.; Alkathiri, T. A.; Alfarraj, A. E.; Alatawi, O. M.; Alkathiri, A. S.; Panneerselvam, C.; Vanaraj, S.; Darwish, A. A. A.; Hamdalla, T. A.; Pasha, A.; Khasim, S. (2022). Green synthesis and characterization of zinc oxide nanoparticles using *Camellia sinensis* tea leaf extract and their antioxidant, anti-bactericidal and anticancer efficacy. *Research on Chemical Intermediates*, *48* (11), 4769–4783. https://doi.org/10.1007/s11164-022-04845-z.

[4] Alamdari, S.; Sasani Ghamsari, M.; Lee, C.; Han, W.; Park, H. H.; Tafreshi, M. J.; Afarideh, H.; Ara, M. H. M. (2020). Preparation and Characterization of Zinc Oxide Nanoparticles Using Leaf Extract of *Sambucus ebulus*. *Applied Sciences*, *10* (10), 3620. https://doi.org/10.3390/app10103620.

[5] Abdelghany, T. M.; Al-Rajhi, A. M. H.; Yahya, R.; Bakri, M. M.; Al Abboud, M. A.; Yahya, R.; Qanash, H.; Bazaid, A. S.; Salem, S. S. (2023). Phytofabrication of zinc oxide nanoparticles with advanced characterization and its antioxidant, anticancer, and antimicrobial activity against pathogenic microorganisms. *Biomass Conversion and Biorefinery*, *13* (1), 417-430. https://doi.org/10.1007/s13399-022-03412-1.

[6] Agarwal, H.; Kumar, S. V.; Rajeshkumar, S. (2017). A review on green synthesis of zinc oxide nanoparticles–An eco-friendly approach. *Resource-Efficient Technologies*, *3* (4), 406–413. https://doi.org/10.1016/j.reffit.2017.03.002.

[7] Adam, F.; Himawan, A.; Aswad, M.; Ilyas, S.; Heryanto; Anugrah, M. A.; Tahir, D. (2021). Green synthesis of zinc oxide nanoparticles using *Moringa oleifera* L. water extract and its photocatalytic evaluation. *Journal of Physics: Conference Series*, *1763* (1), 012002. https://doi.org/10.1088/1742-6596/1763/1/012002.

[8] Rameshraddy; Pavithra, G. J.; Rajashekar Reddy, B. H.; Salimath, M.; Geetha, K. N.; Shankar, A. G. (2017). Zinc oxide nano particles increases Zn uptake, translocation in rice with positive effect on growth, yield and moisture stress tolerance. *Indian Journal of Plant Physiology*, *22* (3), 287-294. https://doi.org/10.1007/s40502-017-0303-2.

[9] Rizwan, M.; Ali, S.; Qayyum, M. F.; Ok, Y. S.; Adrees, M.; Ibrahim, M.; Zia-ur-Rehman, M.; Farid, M.; Abbas, F. (2017). Effect of metal and metal oxide nanoparticles on growth and physiology of globally important food crops: A critical review. *Journal of Hazardous Materials*, *322*, 2-16. https://doi.org/10.1016/j.jhazmat.2016.05.061.

[10] Faizan, M.; Yu, F.; Chen, C.; Faraz, A.; Hayat, S. (2021). Zinc Oxide Nanoparticles Help to Enhance Plant Growth and Alleviate Abiotic Stress: A Review. *Current Protein and Peptide Science*, *22* (5), 362–375. https://doi.org/10.2174/1389203721666201016144848.

[11] Venkatachalam, P.; Jayaraj, M.; Manikandan, R.; Geetha, N.; Rene, E. R.; Sharma, N. C.; Sahi, S. V. (2017). Zinc oxide nanoparticles (ZnONPs) alleviate heavy metal-induced toxicity in *Leucaena leucocephala* seedlings: A physiochemical analysis. *Plant Physiology and Biochemistry*, *110*, 59-69. https://doi.org/10.1016/j.plaphy.2016.08.022.

[12] Agarwal, H.; Shanmugam, V. (2020). A review on anti-inflammatory activity of green synthesized zinc oxide nanoparticle: Mechanism-based approach. *Bioorganic Chemistry*, *94*, 103423. https://doi.org/10.1016/j.bioorg.2019.103423.

[13] Saleem, H.; Usman, A.; Mahomoodally, M. F.; Ahemad, N. (2021). *Bougainvillea glabra* (Choisy): A comprehensive review on botany, traditional uses, phytochemistry, pharmacology and toxicity. *Journal of Ethnopharmacology*, *266*, 113356. https://doi.org/10.1016/j.jep.2020.113356.

[14] Sahu, N.; Saxena, J. (2012). *Bougainvillea glabra* a natural antioxidant: A review. *Inventi Rapid: Planta Activa* (April–June). Publisher record.

[15] Abarca-Vargas, R.; Petricevich, V. L. (2018). Bougainvillea Genus: A Review on Phytochemistry, Pharmacology, and Toxicology. *Evidence-Based Complementary and Alternative Medicine*, *2018* (1), 9070927. https://doi.org/10.1155/2018/9070927.

[16] Samzadeh-Kermani, A.; Izadpanah, F.; Mirzaee, M. (2016). The improvements in the size distribution of zinc oxide nanoparticles by the addition of a plant extract to the synthesis. *Cogent Chemistry*, *2* (1), 1150389. https://doi.org/10.1080/23312009.2016.1150389.

[17] Oves, Mohammad; Rauf, Mohd Ahmar; Qari, Huda A. (2023). Therapeutic Applications of Biogenic Silver Nanomaterial Synthesized from the Paper Flower of *Bougainvillea glabra* (Miami, Pink). *Nanomaterials*, *13* (3), 615. https://doi.org/10.3390/nano13030615.